JACS Au
AN OPEN ACCESS JOURNAL OF THE AMERICAN CHEMICAL SOCIETY

pubs.acs.org/jacsau

Article

Tunable Interfacial Electronic Pd−Si Interaction Boosts Catalysis via Accelerating O_2 and H_2O Activation

Tao Dong,[ξ] Jian Ji,[ξ] Leyi Yu, Pingli Huang, Yiheng Li, Ziyi Suo, Biyuan Liu, Zhuofeng Hu, and Haibao Huang*

Cite This: *JACS Au* 2023, 3, 1230−1240

Read Online

ACCESS | Metrics & More | Article Recommendations | Supporting Information

ABSTRACT: Engineering the interfacial structure between noble metals and oxides, particularly on the surface of non-reducible oxides, is a challenging yet promising approach to enhancing the performance of heterogeneous catalysts. The interface site can alter the electronic and *d*-band structure of the metal sites, facilitating the transition of energy levels between the reacting molecules and promoting the reaction to proceed in a favorable direction. Herein, we created an active Pd−Si interface with tunable electronic metal−support interaction (EMSI) by growing a thin permeable silica layer on a non-reducible oxide ZSM-5 surface (termed Pd@SiO_2/ZSM-5). Our experimental results, combined with density functional theory calculations, revealed that the Pd−Si active interface enhanced the charge transfer from deposited Si to Pd, generating an electron-enriched Pd surface, which significantly lowered the activation barriers for O_2 and H_2O. The resulting reactive oxygen species, including O_2^-, O_2^{2-}, and −OH, synergistically facilitated formaldehyde oxidation. Additionally, moderate electronic metal−support interaction can promote the catalytic cycle of $Pd^0 \leftrightarrows Pd^{2+}$, which is favorable for the adsorption and activation of reactants. This study provides a promising strategy for the design of high-performance noble metal catalysts for practical applications.

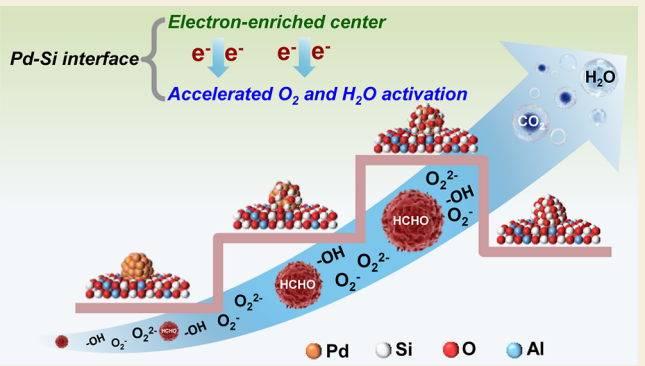

KEYWORDS: *heterogeneous catalysts, Pd−Si active interface, electronic metal−support interaction, formaldehyde oxidation*

INTRODUCTION

Platinum group metals (PGMs) such as Pt, Pd, and Ir are highly efficient heterogeneous catalysts that find widespread application in environmental and energy catalysis.[1−3] The catalytic activity of PGMs is strongly dependent on the nature of the support material, which can be either reducible (TiO_2, CeO_2, FeO_x, MnO_2, MoO_3, etc.) or non-reducible (SiO_2, zeolite, etc.). The significant differences in local electronic structures, unsaturated coordinative metal sites, and structural stability of these two types of supports influence the catalytic performance of PGMs.[4] Therefore, it is critical to rationally design and modulate the geometric and electronic structures on metal oxide surfaces to optimize heterogeneous catalysis. Various strategies have been developed to create defect sites,[5,6] metal−oxide interfaces,[7,8] grain boundaries,[9] and hierarchical pore structures.[10,11] Among them, metal−oxide interfaces are of particular importance since they can induce electronic metal−support interaction (EMSI) by causing charge redistribution at the interface. This can modulate the unoccupied *d* states of noble metal sites and significantly improve reactant adsorption and activation, thereby enhancing catalytic performance.[12−14]

Currently, numerous studies have been conducted to investigate the development of active metal−oxide interfaces for various reactions to achieve exceptional catalytic performance, such as the Au−TiO_2 interface for CO oxidation,[15] Pd−PdO interface for deep oxidation of light alkanes,[16] Cu−ZnO_x interface for steam reforming of methanol,[17] Cu−CeO_2 interface for water−gas shift reaction,[18] and Ni−TiO_2 interface for Fischer−Tropsch synthesis.[19] The active metal−oxide interfaces are expected to provide new catalytic sites that can facilitate the activation/dissociation of O_2 and H_2O, leading to the generation of reactive oxygen species (e.g., O_2^-, O_2^{2-}, O^-, and surface hydroxyl groups) and accelerating the efficiency of catalytic reactions. It is well known that the activation of O_2 and H_2O is a critical step in heterogeneous catalytic oxidation. For example, the activation of O_2 is closely associated with CO oxidation, while the activation of H_2O is closely associated with the water−gas shift reaction.[20−22] For the catalytic oxidation of formaldehyde (HCHO, a typical oxygenated VOC and one of the main indoor gaseous pollutants attracting

Received: February 23, 2023
Revised: March 22, 2023
Accepted: March 23, 2023
Published: April 3, 2023

https://doi.org/10.1021/jacsau.3c00093
JACS Au 2023, 3, 1230−1240

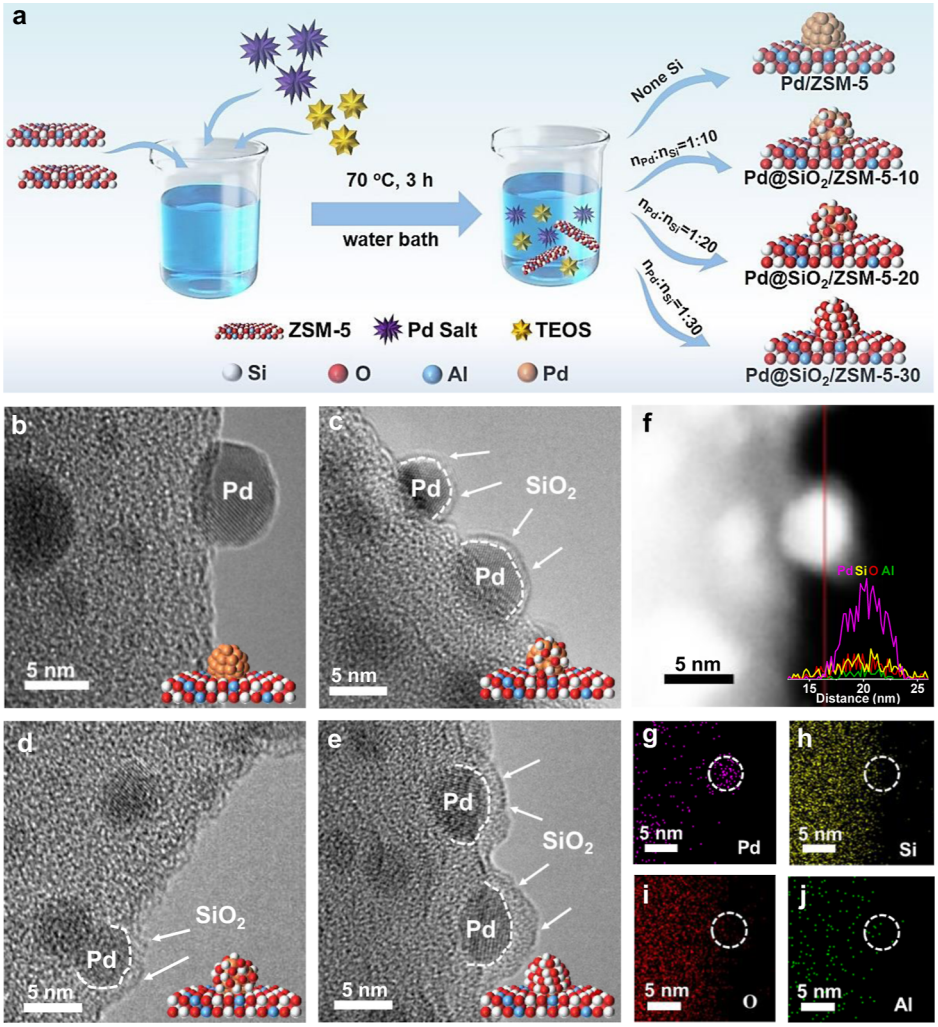

Figure 1. Schematic illustration, morphology, and structural characterization of serial catalysts. (a) Schematic illustration for the synthesis of catalysts. (b) HRTEM images of Pd/ZSM-5 and (c–e) Pd@SiO_2/ZSM-5-X (X = 10, 20, 30). (f) AC-STEM, line scan (inside figure f), and (g–j) AC-EDS mapping of Pd@SiO_2/ZSM-5-20.

increasing attention), the catalytic ability highly depends on the activation of both O_2 and H_2O.[23−25] Therefore, the construction of active interfaces is vital in enhancing electron delocalization and adjusting the *d*-band center of metal sites to form the EMSI effect, which is important for the design and development of efficient HCHO degradation catalysts.

Generally, EMSI can be induced by strong metal−support interaction (SMSI) via charge transfer across the interface. SMSI is usually achieved by thermally treating reducible metal oxide supports at high temperatures (≥500 °C), in a specific atmosphere, such as H_2 or O_2.[26,27] The resulting overlayers formed on the surface of the metal nanoparticles (NPs) can either significantly reduce the catalytic activity for PGM/reducible oxide catalysts by excessively encapsulating active sites or decrease the number of active interfacial sites.[28] Therefore, boosting the interfacial sites through appropriate SMSI is necessary to effectively modulate the strength of EMSI and maintain the accessibility of partial metal surface sites to reactant molecules. While successful cases of tuning EMSI on reducible oxide-supported PGM catalysts have been documented,[20,29] SMSI resulting from reducible metal oxide supports has poor water durability as the oxide overlayers tend to undergo dynamic migration during reactions in a humid atmosphere.[30] In contrast, non-reducible oxide supports such as SiO_2 and zeolites are well-known "inert" supports or shell materials to fabricate core−shell structures, which present excellent hydrothermal stability as well as great moisture resistance.[14] However, these non-reducible oxide supports are too stable to obtain a thin oxide encapsulation layer via ordinary reduction or oxidation treatment at high temperatures. Due to the difficulty of regulating the interface structure on the non-reducible oxide surface, only a few reports have been published on the construction of metal−non-reducible oxide interfaces. Therefore, constructing a stable active interface with tunable EMSI on non-reducible oxides remains a highly necessary yet challenging task.

In this study, we constructed a Pd−Si active interface with tunable EMSI by growing a permeable SiO_2 layer over Pd, which was supported on non-reducible oxide ZSM-5 (termed Pd@SiO_2/ZSM-5). Tuning the EMSI over the Pd@SiO_2/ZSM-5 catalyst resulted in enhanced charge transfer from deposited Si to Pd, which formed an electron-enriched surface of the Pd particles, resulting in significantly improved catalytic activity for HCHO deep oxidation. The optimal catalytic performance of Pd@SiO_2/ZSM-5-20 was attributed to the catalyst's moderate EMSI. This optimizes the *d*-band center of

https://doi.org/10.1021/jacsau.3c00093
JACS Au 2023, 3, 1230−1240

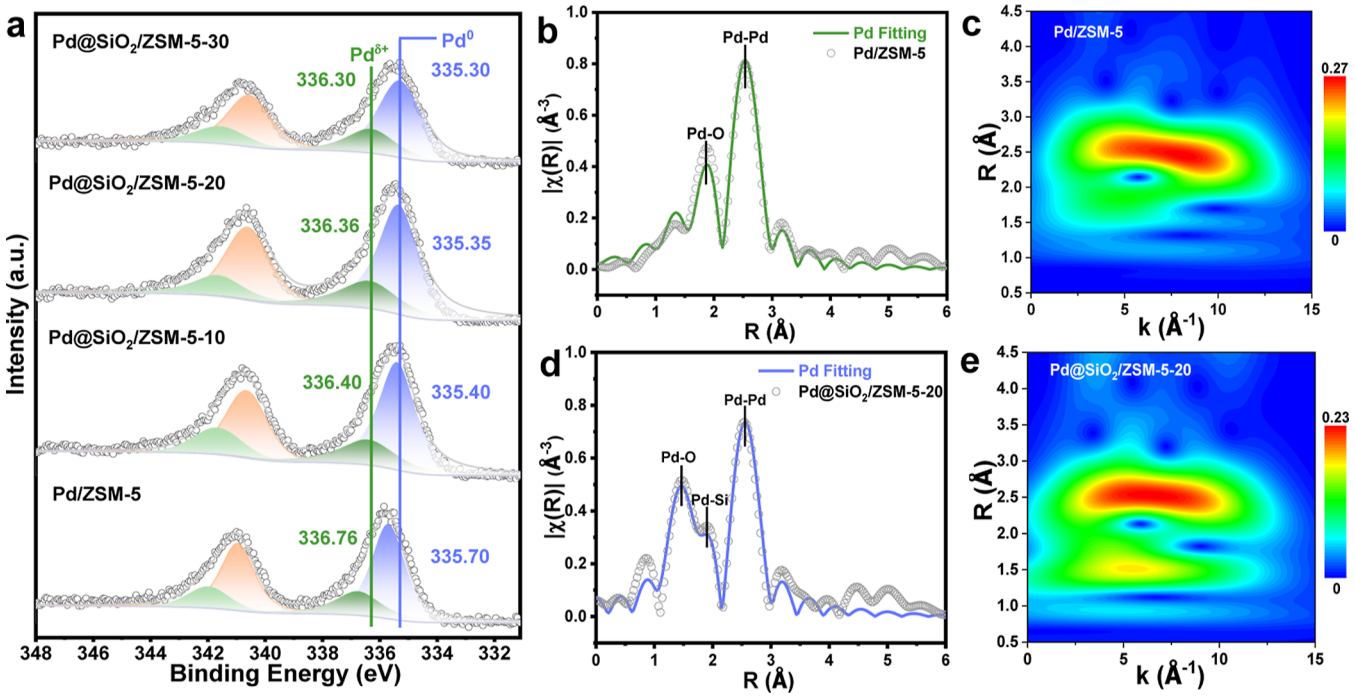

Figure 2. Valence state and Pd−Si interaction of Pd@SiO_2/ZSM-5-20. (a) XPS spectra of Pd 3d for Pd@SiO_2/ZSM-5-X. (b,d) Fourier transform of k^2-weighted EXAFS spectra of Pd/ZSM-5 and Pd@SiO_2/ZSM-5-20 at Pd K-edge shown in R space. (c,e) Wavelet transforms from experimental data for Pd/ZSM-5 and Pd@SiO_2/ZSM-5-20.

interface sites to be closer to the Fermi energy level, which facilitates the adsorption/activation capacities of reactants and intermediates. The experimental results and density functional theory (DFT) calculations revealed that the Pd−Si interface served as new active sites, which significantly improved the activation of O_2 and H_2O to form reactive oxygen species (O_2^-, O_2^{2-}, and −OH). The O_2^-, O_2^{2-}, and −OH species can synergistically promote HCHO oxidation. This work provides a deep understanding of moderate EMSI in non-reducible oxide-supported Pd catalysts and opens up a window for the design of highly active heterogeneous catalysts.

RESULTS AND DISCUSSION

Synthesis and Physicochemical Properties

A series of Pd@SiO_2/ZSM-5-X (where X represents the molar ratio of Pd and Si) were synthesized using a wet chemical method, and a schematic illustration for the synthesis is shown in Figure 1a. X-ray diffraction (XRD) patterns (Figure S1) demonstrate that Pd@SiO_2/ZSM-5-X displays five typical diffraction peaks characteristic of a crystalline MFI structure. Neither peaks characteristic of metallic Pd nor amorphous silica phases are observed due to the low loading or high dispersion of Pd (ca. 0.44 wt % determined by inductively coupled plasma optical emission spectrometry analysis, Table S1) and Si species.

Figure S2 displays that the ZSM-5 are typical hexagonal coffin-shaped crystals. The mean size of Pd NPs in Pd/ZSM-5 is 8.4 nm (Figure S3). Following the introduction of Si species, the mean size is notably reduced to 4.7 nm in Pd@SiO_2/ZSM-5-X (Figures S4−S6). High-angle annular dark-field scanning transmission electron microscopy and elemental energy-dispersive X-ray spectroscopy (EDS) mapping images in Figures S7−S10 indicate the homogeneous distribution of Pd species on the surface of ZSM-5 zeolite. High-resolution transmission electron microscopy (HRTEM) and aberration-corrected scanning transmission electron microscopy (AC-STEM) were further performed to evaluate the morphology and structure of Pd@SiO_2/ZSM-5-X. Figure 1b exhibits the presence of only Pd NPs on Pd/ZSM-5. The addition of TEOS created the oxide overlayers that covered the Pd NPs in Pd@SiO_2/ZSM-5-10 (Figure 1c), Pd@SiO_2/ZSM-5-20 (Figure 1d), and Pd@SiO_2/ZSM-5-30 (Figure 1e), with shell thicknesses of 0.69, 1.21, and 1.73 nm, respectively (Table S2). The AC-STEM image (Figure 1f), line scan (inset of Figure 1f), and AC-EDS mapping (Figure 1g−j) of Pd@SiO_2/ZSM-5-20 clearly indicate that the overlayer is composed of SiO_2. These SiO_2 overlayers did not alter the general pore structure of Pd@SiO_2/ZSM-5-X, which retained type I and IV isotherms (Figure S11), while gradually blocking some pore channels and reducing the external surface area from 199 to 179 $m^2\ g^{-1}$ (Table S1).

The Fourier transform infrared (FT-IR) spectroscopy spectra (Figure S12) showed characteristic peaks of the Si−OH−Al group (3679 cm^{-1}),[31] surface physisorbed water (3324 cm^{-1}),[32,33] Si−O bonds (between 1600 and 650 cm^{-1}),[34] Si−O−T bonds (1215 and 1075 cm^{-1}),[35] Si−OH bond (921 cm^{-1}), and [SiO_4] units (814 cm^{-1}).[34,36] Interestingly, a red shift is observed from 1364 to 1334 cm^{-1} (Si−O stretching vibration) for Pd@SiO_2/ZSM-5-20 and Pd@SiO_2/ZSM-5-30. This shift was attributed to the appropriate introduction of the SiO_2 overlayer, which improves the EMSI between Pd and SiO_2. Since Pd has a higher electronegativity, the electrons would transfer from Si to Pd. This results in a decrease in the electron cloud density on Si and a reduction in the force constant and vibration frequency of Si−O bonds, leading to the observed shift in the absorption peak to a lower wavenumber. Thus, bands at 1364 and 1334 cm^{-1} might be assigned to Si−O stretching vibration on ZSM-5 and Pd−SiO_2 components, respectively.

https://doi.org/10.1021/jacsau.3c00093
JACS Au 2023, 3, 1230−1240

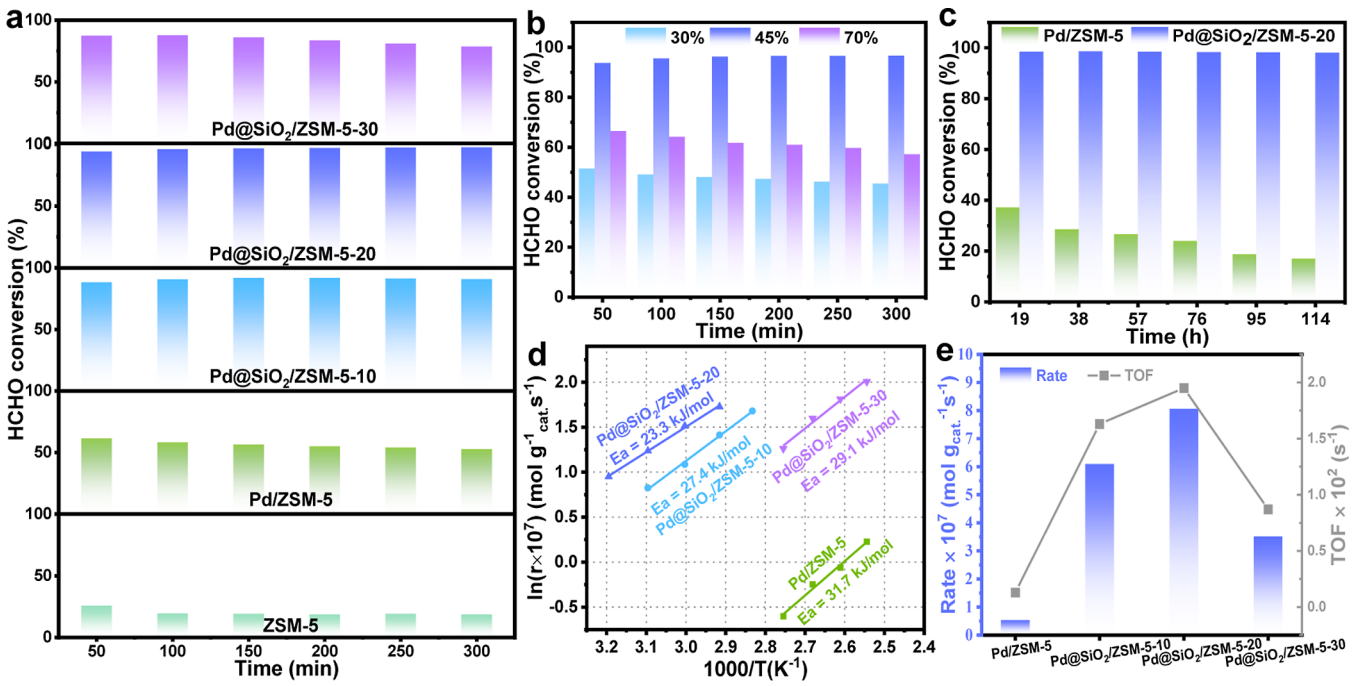

Figure 3. Reaction performance of Pd@SiO_2/ZSM-5-20 and related catalysts. (a) HCHO conversion as a function of time over Pd@SiO_2/ZSM-5-20 and related catalysts. (b) HCHO conversion as a function of time over Pd@SiO_2/ZSM-5-20 in different relative humidities. (c) Stability test of Pd@SiO_2/ZSM-5-20 and Pd/ZSM-5. (d,e) Arrhenius plots, rate, and TOF of Pd@SiO_2/ZSM-5-20 and related catalysts with a WHSV of 2400,000 mL $g_{cat.}^{-1}$ h^{-1}.

X-ray photoelectron spectra (XPS) measurements were performed to study the Pd electronic state and the interaction between Pd and the support. As shown in Figure 2a, the $Pd3d_{5/2}$ peak of the Pd/ZSM-5 sample without the SiO_2 overlayer can be fitted into two peaks at about 336.76 and 335.70 eV, which are attributed to $Pd^{\delta+}$ ($0 < \delta < 2$) and Pd^0 species, respectively.[37−39] For Pd@SiO_2/ZSM-5-X, the peak $Pd3d_{5/2}$ of $Pd^{\delta+}$ and Pd^0 species shifted toward a lower binding energy, indicating the relatively negatively charged Pd surface.[23] The difference in electronic status of Pd species was attributed to the different metal−support interactions. The negatively charged Pd originates from the charge transfer from the SiO_2 overlayers to Pd, which is consistent with the FT-IR results. Notably, the thicker the SiO_2 overlayer, the lower the binding energy of Pd, which is probably due to the electronic interaction between Pd and the SiO_2 overlayer in the Pd−Si interface. This indicates that the electronic interaction between Pd and the SiO_2 overlayer is increased with X, and the strength of EMSI follows the order of Pd@SiO_2/ZSM-5-30 > Pd@SiO_2/ZSM-5-20 > Pd@SiO_2/ZSM-5-10. In addition, the ratio of $Pd^0/(Pd^0 + Pd^{\delta+})$ on the surfaces of the four samples is similar, ∼0.73−0.74 (Table S3). In this case, the catalytic activity of formaldehyde oxidation is not well correlated with the metal Pd^0 reduction degree but with the EMSI effect.

To further investigate the EMSI effect (electronic accessibility and properties of Pd species), CO-adsorption diffuse reflectance infrared Fourier transform spectroscopy (DRIFTS) was conducted. As shown in Figure S13, the bands at 2094 cm^{-1} can be assigned to the linear adsorption of CO on Pd^0 NPs over the Pd/ZSM-5 sample.[40,41] After the SiO_2 overlayer was constructed, a red shift from 2094 to 2087 cm^{-1} was observed, unambiguously demonstrating the presence of negatively charged Pd species due to charge transfer from the SiO_2 overlayers to Pd.[23,40] Furthermore, the adsorption strength of CO is compared to study the status of exposed active sites. Pd/ZSM-5 has the lowest CO adsorption strength, indicating the lower exposure of Pd sites due to the large size of Pd NPs (8.4 nm). After the introduction of Si species, the CO adsorption strength on the Pd@SiO_2/ZSM-5-10 surface increased, demonstrating that Pd sites were more exposed because of the smaller size of Pd NPs (4.7 nm). The aforementioned results highlight the beneficial role of SiO_2 overlayers in increasing the Pd dispersion, and the SiO_2 overlayer is possibly permeable due to the existence of gaps or pores on the overlayers. Additionally, the CO adsorption strengths of Pd@SiO_2/ZSM-5-20 and Pd@SiO_2/ZSM-5-30 are further enhanced with the increase of the SiO_2 overlayer, possibly because the EMSI over Pd@SiO_2/ZSM-5-30 is stronger than that of Pd@SiO_2/ZSM-5-20 and the SiO_2 overlayer is permeable. Consequently, Pd@SiO_2/ZSM-5-30 exhibited the strongest CO adsorption strength, and Pd@SiO_2/ZSM-5-20 had a moderate CO adsorption strength corresponding to a moderate EMSI. The moderate EMSI may be favorable to the activation of O_2 and H_2O for promoting HCHO oxidation, which has been supported by recent studies.[29] The subsequent activity test of HCHO oxidation revealed that Pd@SiO_2/ZSM-5-20 exhibited the best catalytic performance (detailed analysis will be discussed soon).

X-ray absorption near-edge structure (XANES) and extended X-ray absorption fine structure (EXAFS) studies were employed to obtain further insights into the elemental coordination, electronic state, and bonding structure between Pd and the SiO_2 overlayer in Pd@SiO_2/ZSM-5-20 and Pd/ZSM-5. The EXAFS fitting data are summarized in Table S4. As shown in Figure S14a, the Pd K-edge XANES spectra of Pd@SiO_2/ZSM-5-20 and Pd/ZSM-5 are similar to the Pd foil reference spectra, indicating that the metal Pd species (Pd^0) are the dominant Pd species in both samples. Significantly, a

https://doi.org/10.1021/jacsau.3c00093
JACS Au 2023, 3, 1230−1240

smaller shift of the Pd K-edge absorption to the lower binding energy for Pd@SiO_2/ZSM-5-20 compared to Pd/ZSM-5 suggests that the Pd atoms in Pd@SiO_2/ZSM-5-20 might possess a higher electron density.[42,43] This indicates that the introduction of Si species induces charge transfer from Si to Pd, forming an electron-enriched surface of Pd NPs in Pd@SiO_2/ZSM-5-20, which is consistent with XPS and CO-DRIFTS results. In the Pd K-edge Fourier transformed EXAFS spectra of Pd/ZSM-5 (Figures 2b, S14b, and Table S4), two forms of bonding are observed: Pd−O and Pd−Pd, with lengths of ∼1.92 and ∼2.71 Å, respectively. In the Pd@SiO_2/ZSM-5-20 sample (Figures 2d, S14b, and Table S4), a new peak at ∼2.22 Å could be assigned to Pd−Si, indicating the construction of the Pd−Si interface. Furthermore, as shown in Table S4, the bond lengths of Pd−O (∼1.99 Å) and Pd−Pd (∼2.76 Å) over Pd@SiO_2/ZSM-5-20 are slightly longer than those of Pd/ZSM-5, suggesting a higher electron density of Pd atoms in Pd@SiO_2/ZSM-5-20.[43] The signal intensities of Pd@SiO_2/ZSM-5-20 are stronger and broader than Pd/ZSM-5 at R = ∼1.0−2.0 Å, as seen from the wavelet transform plot (Figure 2c,e), due to the coexistence of Pd−O and Pd−Si bonds. The formation of Pd−Si bonds is most likely the result of a mechanism proposed by Duprez et al.[44] in which hydrogen spillover from metal to oxide reduces silica to Si^0, which further migrates to the near surface of Pd NPs[45,46] as follows: (i) Pd−O_{inter}−Si−O−Si−O → Pd−Si_{inter}−O−Si−O + 1/2O_2 (g); (ii) 1/2O_2 (g) + H_2 (g) → H_2O (g). Therefore, based on the results of FT-IR, XPS, CO-DRIFTS, XANES, EXAFS, and wavelet transform plots, it can be fully deduced that the Pd−Si interface is successfully constructed through modulation of moderate EMSI between Pd and the permeable SiO_2 overlayer on Pd@SiO_2/ZSM-5-20. The Pd−Si interface improves the transfer of charge from Si to Pd and forms an electron-enriched surface of Pd NPs, providing new active sites to enhance the catalytic efficiency.

Deep Oxidation Performance

The catalytic performance of Pd@SiO_2/ZSM-5-20 and related catalysts for HCHO oxidation was evaluated in an air flow containing 100 ppm HCHO, where the weight hourly space velocity (WHSV) and relative humidity (RH) were 100,000 mL $g_{cat.}^{-1}$ h^{-1} and 45%, respectively. As shown in Figures 3a and S15, the HCHO oxidation activity of ZSM-5 zeolite is below 20%, with a CO_2 selectivity of only ∼8%. This result can be attributed to the adsorption of ZSM-5 and the activation of HCHO by surface hydroxyl species of ZSM-5, as observed by FT-IR spectra in Figure S12a. After Pd NPs were supported on ZSM-5 (Pd/ZSM-5), HCHO conversion reached 60% at 50 min while gradually declining to 50% after 300 min, indicating unsatisfactory catalytic activity and stability. As the SiO_2 overlayer was constructed on the Pd/ZSM-5 catalyst, it significantly improved the HCHO oxidation activity. The enhanced performance was likely due to the effective dispersion of Pd species and the construction of EMSI between Pd and SiO_2, which facilitated electronic transfer from Si to Pd. The amount of SiO_2 introduced, however, did not proportionally increase the catalytic activity. The HCHO oxidation activity increases and then decreases with increased SiO_2 overlayer thickness, with Pd@SiO_2/ZSM-5-20 demonstrating the best activity. The optimum catalytic performance was obtained with an appropriate thickness of the SiO_2 overlayer, while excessive SiO_2 leads to blocked access to active sites due to the too strong EMSI effect. Therefore, it can be deduced that moderate EMSI is vital to catalytic activity. Meanwhile, the Pd−Si interface was expected to provide new active sites to improve the activation of O_2 and H_2O, leading to the formation of reactive oxygen species and the acceleration of HCHO degradation.

Generally, water molecules can play a crucial role in the oxidation of HCHO by providing surface hydroxyl groups (−OH) through activation by active sites. These hydroxyl groups can aid in the degradation of intermediates such as DOM and formate. To investigate the impact of RH on HCHO oxidation, the activity of Pd@SiO_2/ZSM-5-20 was tested under varying RH conditions. As shown in Figure 3b, Pd@SiO_2/ZSM-5-20 shows the highest activity of HCHO oxidation at a RH of 45%, compared to 30 and 70%. This result verified that moderate humidity levels are more favorable for HCHO degradation. It might be that low humidity cannot provide sufficient surface hydroxyl groups for HCHO oxidation, leading to the accumulation of intermediates and thus declining the catalytic activity. Similarly, high levels of water can also occupy active sites and reduce catalyst performance due to competitive adsorption between water and HCHO. Furthermore, the durability of Pd@SiO_2/ZSM-5-20 and Pd/ZSM-5 was tested for 114 h (RH = 45%). As shown in Figure 3c, the HCHO conversion over Pd@SiO_2/ZSM-5-20 is still maintained at ∼98%, while Pd/ZSM-5 shows a continuous decrease in conversion over time. This finding suggests that Pd@SiO_2/ZSM-5-20 has superior durability compared to Pd/ZSM-5, which may be attributed to the moderate EMSI for better adsorption and degradation of intermediates. We further compared the HCHO oxidation activities of Pd@SiO_2/ZSM-5-20 with the literature (Table S5), which shows that Pd@SiO_2/ZSM-5-20 has satisfactory catalytic activity and stability for HCHO oxidation.

Additionally, kinetic testing was conducted to further investigate the catalytic performance of Pd@SiO_2/ZSM-5-20 and other related catalysts at high WHSV (2400, 000 mL $g_{cat.}^{-1}$ h^{-1}) and low conversion of less than 15%. Intrinsic kinetic testing was conducted to exclude internal and external diffusion effects, and the Weisz−Prater criterion (C_{WP}) and Mears' criterion (C_M) were used as criteria. $C_{WP} < 1$ and $C_M < 0.15$ indicate negligible internal and external diffusion effects.[16,47−49] The calculation results presented in Tables S6 and S7 indicated that mass transfer limitations were negligible. As shown in Figure 3d,e and Table S8, Pd@SiO_2/ZSM-5-20 exhibits the lowest apparent activation energies (E_a = 23.3 kJ mol^{-1}) compared with the other three samples, and its reaction rate (r) and turnover frequency (TOF) for HCHO oxidation are the highest at 90 °C and are approximately 15 times higher than Pd/ZSM-5. These findings suggest that Pd@SiO_2/ZSM-5-20 is the most effective catalyst based on its catalytic activity, stability, and kinetic tests for HCHO oxidation compared to other samples.

Further investigations were conducted to assess the adaptability of Pd@SiO_2/ZSM-5-20 in other reaction systems. Methane (1500 ppm) and toluene (1000 ppm) were chosen as model compounds to evaluate the catalytic activity of Pd@SiO_2/ZSM-5-20 and Pd/ZSM-5 toward light alkanes and aromatic hydrocarbons, respectively. The flow velocity and WHSV were kept constant at 30 mL min^{-1} and 36,000 mL $g_{cat.}^{-1}$ h^{-1}, respectively, and detailed testing processes are presented in the Supporting Information. As shown in Figure S16, the catalytic activity of Pd@SiO_2/ZSM-5-20 toward methane oxidation is significantly higher than that of Pd/ZSM-

https://doi.org/10.1021/jacsau.3c00093
JACS Au 2023, 3, 1230−1240

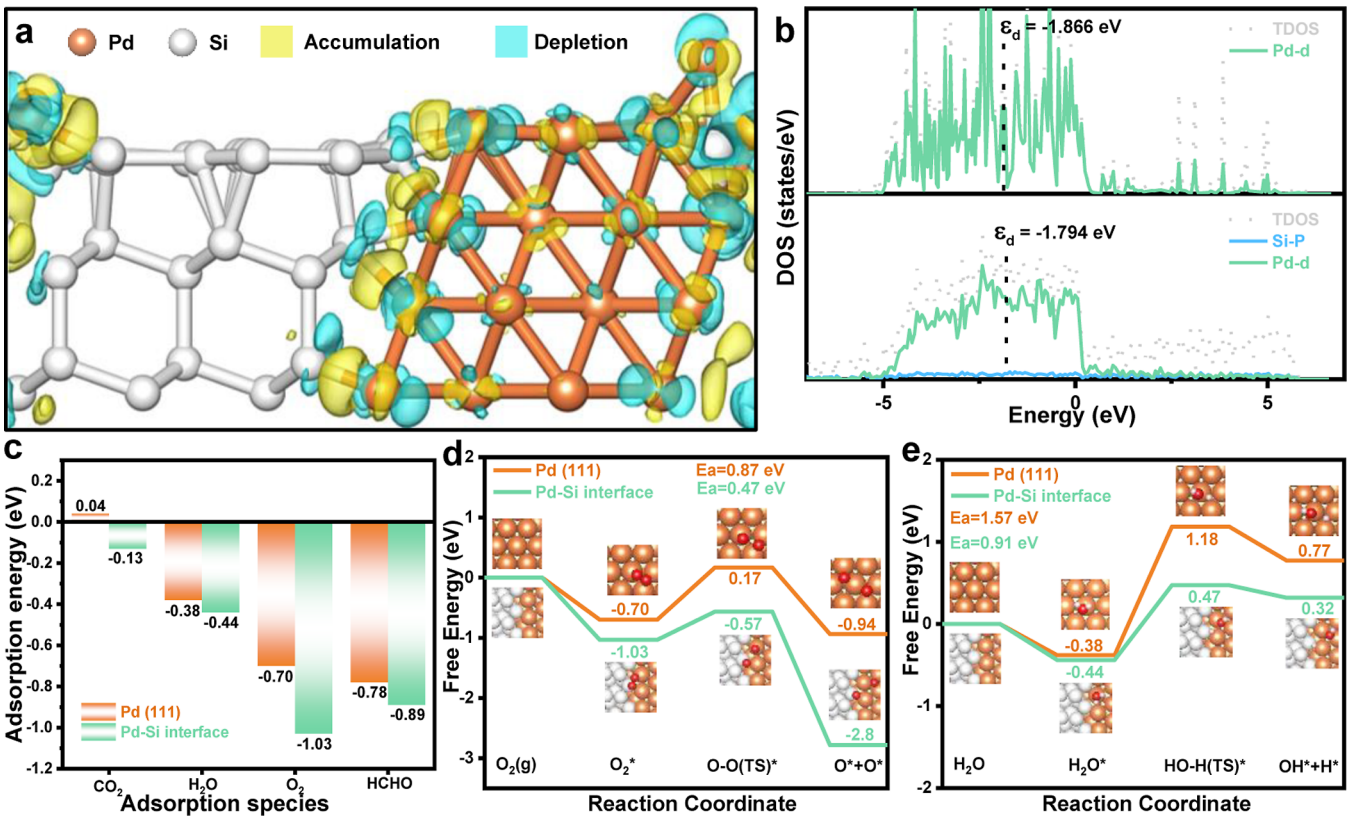

Figure 4. DFT calculations. (a) Charge density distributions among Pd and Si atoms over the Pd−Si interface. (b) Total density of states of Pd(111) and Pthe d−Si interface. (c) Adsorption energy of HCHO, O_2, H_2O, and CO_2 over Pd(111) and the Pd−Si interface. (d,e) Calculated reaction energy profiles of O_2 and H_2O over Pd(111) and the Pd−Si interface.

5. The T_{50} and T_{90} (the reaction temperatures at which 50 and 90% of CH_4 are converted, respectively) are only 264 and 303 °C over Pd@SiO_2/ZSM-5-20, showing the exceptional catalytic activity toward methane oxidation. Likewise, the toluene oxidation activity (Figure S17) of Pd@SiO_2/ZSM-5-20 is also higher than that of Pd/ZSM-5. These results confirmed that the active interface construction strategy is widely applicable in other reaction systems and has a broad range of applicability.

Identifying the Origin of the High Activity

To identify the primary reasons for the optimal catalytic performance of Pd@SiO_2/ZSM-5-20, the valence state change of Pd species, reducibility, metal dispersion, electron distribution, and oxygen and water activation ability were studied. XPS was performed for samples after the HCHO oxidation test (noted as Pd@SiO_2/ZSM-5-20-used and Pd/ZSM-5-used) to investigate the valence changes of Pd species over Pd@SiO_2/ZSM-5-20 and Pd/ZSM-5 during oxidation of HCHO. As shown in Figure S18, the valence of Pd species (Pd^0 and $Pd^{\delta+}$) remains unchanged over Pd@SiO_2/ZSM-5-20-used, while a new peak is detected around 337.62 eV in the $Pd3d_{5/2}$ spectra of the used Pd/ZSM-5 sample, indicating the presence of Pd^{2+} species.[16] Furthermore, the ratio of $Pd^0/(Pd^0 + Pd^{\delta+} + Pd^{2+})$ slightly decreased from 0.74 to 0.68 over Pd@SiO_2/ZSM-5-20-used, while the ratio sharply declined from 0.73 to 0.45 over Pd/ZSM-5-used (Table S9). This implied that the Pd@SiO_2/ZSM-5-20 has excellent oxidation resistance at low temperatures owing to the interface confinement effect of the Pd−Si interface and satisfactory redox ability, which is beneficial to the transition of $Pd^0 \leftrightarrows Pd^{2+}$. Thus, Pd@$SiO_2$/ZSM-5-20 maintained high conversion of HCHO oxidation and exhibited excellent durability.

H_2-TPR tests were carried out to investigate the redox properties of Pd@SiO_2/ZSM-5-20 and related samples. As is well known, Pd NPs were obtained by reducing PdO_x in the presence of H_2, and H_2 could be absorbed on the Pd NPs' surfaces to form PdH_x species. PdH_x species will be decomposed into hydrogen atoms and Pd NPs as the temperature increases. Therefore, the positive reduction peaks at 28−150 °C are assigned to the reduction of Pd^{2+} to Pd^0 (Figure S19), while the negative reduction peaks at 40−100 °C could be attributed to the decomposition of PdH_x.[36,50] The peaks at 200−350 and 350−500 °C corresponded to the reduction of small and large PdO_x particles, respectively.[36] In particular, Pd@SiO_2/ZSM-5-20 exhibited the lowest reduction peak (Pd^{2+} to Pd^0) and decomposition peak (PdH_x), indicating optimal reducibility of Pd@SiO_2/ZSM-5-20 compared to the other three samples. The CO pulse chemisorption test was further performed to study the metal Pd dispersion and CO uptake. As the SiO_2 shell increased (Figure S20 and Table S10), the CO uptake and metal dispersion initially increased and then decreased, and Pd@SiO_2/ZSM-5-20 has the largest CO uptake and highest dispersion.

O_2-temperature-programed oxidation, electron paramagnetic resonance (EPR) spectroscopy, O_2-DRIFTS, and H_2O-DRIFTS were used to study Pd-PdO_x transformation and activation capacity of gaseous O_2 and H_2O. As shown in Figure S21, the negative peaks at 50−250 °C are attributed to the desorption of adsorbed oxygen species.[51,52] The desorption temperature of Pd@SiO_2/ZSM-5-20 (144 °C) is the lowest, suggesting the optimum activation capacity of gaseous oxygen.

https://doi.org/10.1021/jacsau.3c00093
JACS Au 2023, 3, 1230−1240

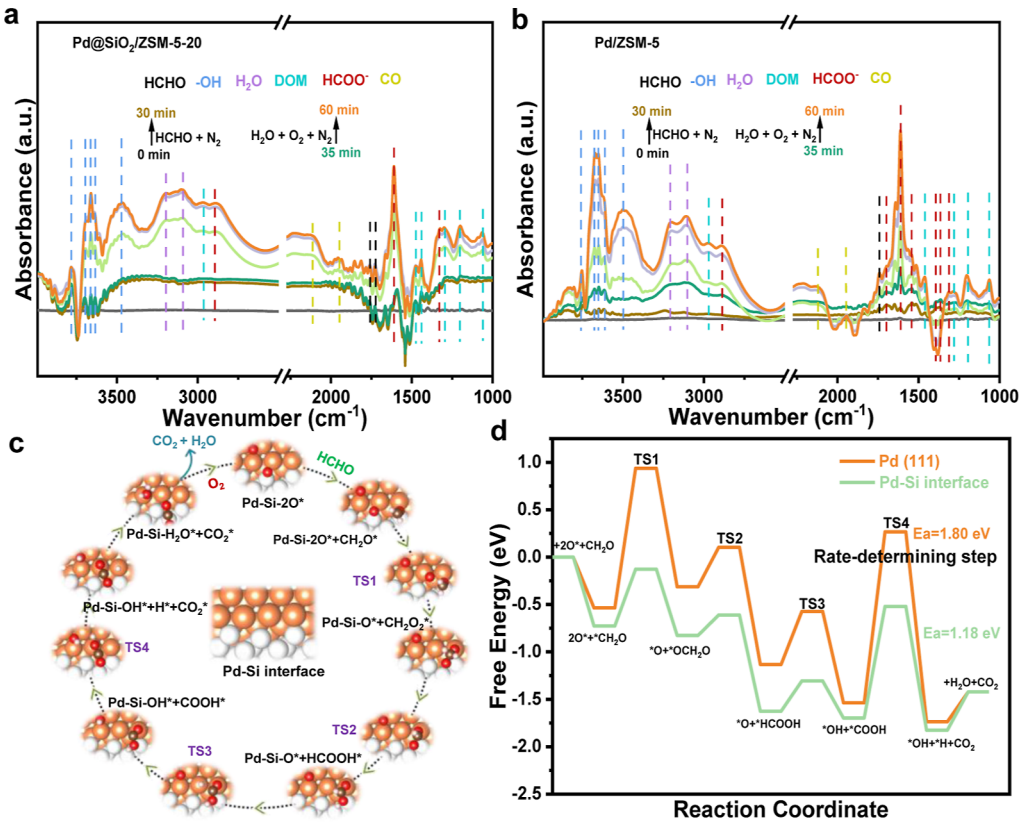

Figure 5. In situ DRIFTS spectra and calculated reaction mechanism of HCHO oxidation. (a,b) In situ DRIFTS spectra collected during HCHO oxidation over Pd@SiO_2/ZSM-5-20 and Pd/ZSM-5 at 25 °C. (c) Possible reaction pathways of HCHO oxidation over the Pd−Si interface. (d) Calculated reaction energy profiles of HCHO oxidation over Pd(111) and the Pd−Si interface.

The oxygen consumption peak at 303 °C could be attributed to the reoxidation of metal Pd species to PdO_x species, and the peak at 807 °C could be assigned to the decomposition of PdO_x species.[51,52] As shown in Figure S22, the *g* value of 2.018 could be attributed to the superoxide (O_2^-) species.[53] To gain a deeper insight into the changes of reactive oxygen species on catalyst surfaces, O_2-DRIFTS adsorption spectra were measured, as shown in Figure S23. It can be observed that the bands at 1050, 1054, and 996 cm^{-1} belong to O_2^- species,[54] which is consistent with the EPR results. Furthermore, peroxide (O_2^{2-}) species could be observed at 870 and 875 cm^{-1}.[54] The relative intensity of the peaks of O_2^- and O_2^{2-} over Pd@SiO_2/ZSM-5-20 is stronger than Pd/ZSM-5 (Figure S24), indicating the better activation capacity of gaseous oxygen over Pd@SiO_2/ZSM-5-20. In H_2O-DRIFTS (Figure S25), the bands at 3800−3400 and 3400−3000 cm^{-1} could be assigned to the vibrational peaks of the surface hydroxyl group (−OH) and adsorbed H_2O, respectively.[32,33,55,56] The relative intensity of −OH is gradually increased, and the peak intensity of −OH over Pd@SiO_2/ZSM-5-20 is also stronger than Pd/ZSM-5, as presented in Figure S26. These results suggested that Pd@SiO_2/ZSM-5-20 has a better activation capacity for gaseous O_2 and H_2O. It might be because electron delocalization at the Pd−Si active interface accelerates O_2 and H_2O activation to form active species (O_2^-, O_2^{2-}, and −OH), which then promote HCHO oxidation. The oxidation activity of HCHO over Pd@SiO_2/ZSM-5-20 and Pd/ZSM-5 is both poor in the test under O_2-alone (without H_2O) and H_2O-alone (without O_2), as shown in Figures S27, S28. Therefore, O_2^-, O_2^{2-}, and −OH active species formed by the simultaneous activation of O_2 and H_2O synergistically promote HCHO oxidation.

The DFT calculation was performed to further elucidate the role of the Pd−Si interface in enhancing the intrinsic catalytic activity. The EXAFS results have proven the existence of the Pd−Si interface, and thus, in this work we are constructing the interface model based on the Pd−Si bonds. Detailed calculation processes and optimal structure models (Figure S29) are presented in the Supporting Information. As shown in Figure 4a, the interaction between Pd and Si atoms is revealed by the calculated electron density. The charges accumulated around the Pd atom in comparison with the Si atom at the Pd−Si interface, and the electron transfer number is 8.335 e, suggesting significant charge delocalization (Si → Pd). Moreover, the electronic interplay of Pd(111) and the Pd−Si interface was further investigated using the total density of states as shown in Figure 4b. The *d*-band center of the Pd−Si interface (−1.794 eV) is closer to the Fermi energy level than that of Pd(111) (−1.866 eV), indicating enhanced adsorption of molecules at the Pd−Si interface. The adsorption energy (E_{ad}) of O_2 and H_2O over the Pd−Si interface is higher than that over Pd(111) (see Figure 4c and Table S11), suggesting that O_2 and H_2O are more easily activated at the Pd−Si interface. Furthermore, the free energy profiles of O_2 (Figure 4d and Table S11) and H_2O (Figure 4e and Table S11) provide insights into the activation reaction path over Pd(111) and the Pd−Si interface. The Pd−Si interface is stronger in the adsorption of O_2 and H_2O than Pd(111) in the first step, indicating the enhanced adsorption and activation ability of O_2 and H_2O molecules caused by the electron enrichment of the

https://doi.org/10.1021/jacsau.3c00093
JACS Au 2023, 3, 1230−1240

interface structure. The dissociation energy barrier of O_2 and H_2O was effectively reduced at the Pd−Si interface, and the activation energy (E_a) of O_2 and H_2O on the Pd−Si interface is lower compared with Pd(111). This is because at the Pd−Si interface, the p-orbital electrons of Si transfer to the unoccupied d-orbital of Pd, raising the energy level of the d-orbital and reducing the activation energy barrier for O_2 and H_2O. Therefore, the experimental results and DFT calculations unambiguously demonstrate that the construction of moderate EMSI is more conducive to the oxidation of HCHO due to the optimal dispersion and redox capacity. The Pd−Si active interface could effectively regulate the surface electronic structure and provide new active sites to accelerate the activation of O_2 and H_2O for boosting HCHO degradation.

Reaction Mechanism of HCHO Oxidation

HCHO oxidation mechanisms on Pd@SiO_2/ZSM-5-20 and Pd/ZSM-5 samples were investigated at 25 °C using in situ DRIFTS. The detailed measurement procedures are described in the Supporting Information, and the results are summarized in Table S12. As shown in Figure 5a, upon exposure to N_2 gas containing 100 ppm HCHO for 30 min, a series of adsorption peaks were observed. The bands in the range of 3782−3469 cm^{-1} are associated with the surface −OH groups,[55,56] and those in the range of 1759−1723 cm^{-1} are assigned to the carbonyl group (C═O) of molecularly adsorbed HCHO.[57,58] Moreover, a weak peak at 1610 cm^{-1} corresponding to the carbonyl group (C═O) of formate ($HCOO^-$) was also observed.[4,58] This suggests that HCHO molecules can be oxidized to $HCOO^-$ species by surface −OH groups over the Pd@SiO_2/ZSM-5-20 surface in the absence of O_2 and H_2O.

After Pd@SiO_2/ZSM-5-20 is exposed to the gas mixture of O_2 + H_2O + N_2, the peak intensity of surface −OH groups increased gradually, demonstrating that H_2O can be activated to form surface −OH on the catalyst surface. The bands in the range of 3197−3090 cm^{-1} are attributed to the generation of H_2O.[59] In addition, the peak intensities of DOM and $HCOO^-$ both increased, and a series of new peaks of DOM (2962, 1294, 1202, and 1060 cm^{-1})[55,56,60−62] and $HCOO^-$ (2892 and 1329 cm^{-1})[61−63] were observed, suggesting that the introduction of O_2 and H_2O can promote HCHO oxidation. Weak peaks at 2113 and 1946 cm^{-1} are assigned to the CO species[63,64] adsorbed on Pd due to the disproportionation reaction that occurred on the catalyst surface. Consequently, HCHO oxidation on Pd@SiO_2/ZSM-5-20 occurs through two reaction pathways. The main reaction path (rapid path) is HCHO → DOM → $HCOO^-$ → CO_2 and the side reaction path is HCHO → DOM → $HCOO^-$ → CO → CO_2. As shown in Figure 5b, the same in situ DRIFTS experiments were measured over Pd/ZSM-5, and similar reaction pathways were observed for HCHO oxidation. However, the band intensities of intermediate species CO and $HCOO^-$ are stronger on Pd/ZSM-5 than on Pd@SiO_2/ZSM-5-20 (Figures S30, S31). This finding indicates that the introduction of the SiO_2 overlayer is beneficial for the adsorption and dissociation of intermediate species due to the moderate EMSI resulting from the Pd−Si interface.

Based on the in situ DRIFTS results, the HCHO oxidation on Pd@SiO_2/ZSM-5-20 and Pd/ZSM-5 follows the Langmuir−Hinshelwood mechanisms. To gain further insights into the reaction mechanisms of HCHO oxidation over Pd@SiO_2/ZSM-5-20 and Pd/ZSM-5, we performed DFT calculations to determine the reaction pathways and free energy of HCHO oxidation. The Pd−Si interface and Pd(111) serve as stable models for calculations, and the detailed calculation processes are presented in the Supporting Information. As shown in Figure 5c, the results show that the first step in the reaction is the adsorption of O_2 and HCHO on the Pd−Si interface surface, which is followed by the activation of these species into O* and CH_2O* species. The CH_2O* species then react with O* to form CH_2O_2* species, which are further transformed into HCOOH* species. Finally, the COOH* species is obtained by the reaction of HCOOH* and O*, which further react with OH* to form CO_2 and H_2O. The reaction pathways of HCHO oxidation over Pd(111) are similar and presented in Figure S32. The rate-determining step was found to be the degradation of COOH* species, as demonstrated by the highest energy barrier among the four transition states (TS4), as shown in Figure 5d. In addition, the E_a = 1.18 eV of TS4 over the Pd−Si interface is lower than that of Pd(111) (E_a = 1.80 eV), suggesting that the HCHO oxidation is easier to proceed on the Pd−Si interface compared to that on Pd(111). Therefore, the experiment results and DFT calculations clearly show that the Pd−Si active interface can promote HCHO oxidation, and the promotion effects can be attributed to the enhancement of O_2 and H_2O adsorption and activation by the formed Pd−Si interface.

CONCLUSIONS

In summary, the Pd−Si active interface with tunable EMSI has been constructed by modulating the permeable SiO_2 overlayer. Various characterization techniques, activity tests, and DFT calculations showed that Pd@SiO_2/ZSM-5-20 has the optimal redox ability, catalytic activity, and durability during HCHO oxidation. Surprisingly, Pd@SiO_2/ZSM-5-20 has the highest r and TOF, ∼15 times higher than Pd/ZSM-5. The optimal catalytic performance is assigned to the catalyst with moderate EMSI, which facilitates the adsorption/activation of reactants and intermediates. The Pd−Si interface provides new active sites to enhance the charge transfer from Si to Pd and form an electron-enriched surface, thereby significantly promoting O_2 and H_2O activation to generate reactive oxygen species. In situ DRIFTS experiment and DFT calculation results demonstrated that the reactive oxygen species O_2^-, O_2^{2-}, and −OH synergistically promote formaldehyde oxidation. The reactants and intermediates are easier to be adsorbed and dissociated on the Pd−Si active interface of Pd@SiO_2/ZSM-5-20 compared with Pd/ZSM-5. Therefore, the interfacial construction strategy can provide a guideline for the rational design of high-performance catalysts.

METHODS

Catalyst Synthesis

Pd@SiO_2/ZSM-5-X (where X represents the molar ratio of Pd and Si) were synthesized by a wet chemical method. First, ZSM-5 (n_{Si}/n_{Al} = 200), $Pd(NO_3)\cdot 2H_2O$, and TEOS were added to a beaker containing 140 mL of H_2O, and the solution was then transferred to a water bath (70 °C) for 3 h. Subsequently, Pd@SiO_2/ZSM-5-X were obtained by successively treating the solid samples with N_2 and H_2/Ar mixed gases at a suitable temperature, and the detailed preparation procedures are presented in the Supporting Information.

Characterization Methods

XRD, inductively coupled plasma optical emission spectrometry, FT-IR spectroscopy, N_2 adsorption/desorption analysis, TEM, HRTEM, EDS elemental mapping, AC-TEM, AC-EDS elemental mapping, XPS, electron paramagnetic resonance (EPR) spectroscopy, CO pulse

https://doi.org/10.1021/jacsau.3c00093
JACS Au 2023, 3, 1230−1240

chemisorption, XANES study, EXAFS study, H_2-temperature programed reduction (H_2-TPR), O_2-temperature-programed oxidation, and in situ DRIFTS characterization tests were used to measure the physical and chemical performance, as well as the plausible reaction mechanism, of Pd@SiO_2/ZSM-5-20 and related samples. The Supporting Information describes the detailed testing processes.

Activity and Kinetic Tests

Formaldehyde (HCHO, 100 ppm) oxidation was performed in a continuous-flow fixed-bed reactor (internal diameter 8 mm). The WHSV and RH values were fixed at 100,000 mL $g_{cat.}^{-1}$ h^{-1} and 45%, respectively. The HCHO and CO_2 concentrations were measured by a multigas analyzer (Gasera One, Gasera Ltd., Finland). The kinetic test used 210 ppm HCHO/air with a WHSV of 2,400,000 mL $g_{cat.}^{-1}$ h^{-1} and 3 mg of the catalyst mixed with 47 mg of inert quartz sand (40−60 mesh) for each testing while internal and external diffusion were removed. The HCHO conversions were controlled within 15%. The Supporting Information contains the results of the detailed activity and kinetic tests.

DFT Calculations

The adsorption energy (E_{ad}), activation energy (E_a), and reaction mechanisms of O_2, H_2O, and HCHO with two different models, including Pd(111) and the Pd−Si interface, are studied by DFT calculations. The detailed calculation methods are provided in the Supporting Information.

■ ASSOCIATED CONTENT

Supporting Information

The Supporting Information is available free of charge at https://pubs.acs.org/doi/10.1021/jacsau.3c00093.

Additional experimental details, characterization, catalytic activity results, computational methods, and additional data (PDF)

■ AUTHOR INFORMATION

Corresponding Author

Haibao Huang − *School of Environmental Science and Engineering, Sun Yat-sen University, Guangzhou 510006, China;* orcid.org/0000-0002-9259-7179; Email: seabao8@gmail.com

Authors

Tao Dong − *School of Environmental Science and Engineering, Sun Yat-sen University, Guangzhou 510006, China*

Jian Ji − *School of Environmental Science and Engineering, Sun Yat-sen University, Guangzhou 510006, China; Guangdong Academy of Sciences, Institute of Chemical Engineering, Guangzhou 510665, China*

Leyi Yu − *School of Environmental Science and Engineering, Sun Yat-sen University, Guangzhou 510006, China*

Pingli Huang − *School of Environmental Science and Engineering, Sun Yat-sen University, Guangzhou 510006, China*

Yiheng Li − *School of Environmental Science and Engineering, Sun Yat-sen University, Guangzhou 510006, China*

Ziyi Suo − *School of Environmental Science and Engineering, Sun Yat-sen University, Guangzhou 510006, China*

Biyuan Liu − *School of Environmental Science and Engineering, Sun Yat-sen University, Guangzhou 510006, China*

Zhuofeng Hu − *School of Environmental Science and Engineering, Sun Yat-sen University, Guangzhou 510006, China;* orcid.org/0000-0002-7879-6446

Complete contact information is available at: https://pubs.acs.org/10.1021/jacsau.3c00093

Author Contributions

H.H., T.D., and J.J. conceived the research idea and designed the experiments. T.D. and J.J. performed all the experiments and analyzed all the data. L.Y., P.H., Y.L., and B.L. participated in the synthesis of samples and characterization. Z.S. drew the Table of Contents (TOC). Z.H. performed the DFT calculations.

Author Contributions

$^{\xi}$T.D. and J.J. contributed equally to this work. All authors discussed the results and approved the final version of the manuscript.

Notes

The authors declare no competing financial interest.

■ ACKNOWLEDGMENTS

This work was supported by the National Natural Science Foundation of China (22076224 and 22276223) and Guangdong Basic and Applied Basic Research Foundation (2022A1515010241). The theoretical calculation was supported by the National supercomputer center in Guangzhou and National Supercomputing Center in Shenzhen (Shenzhen Cloud Computing Center).

■ REFERENCES

(1) Zhang, S.; Liu, Y.; Zhang, M.; Ma, Y.; Hu, J.; Qu, Y. Sustainable production of hydrogen with high purity from methanol and water at low temperatures. *Nat. Commun.* **2022**, *13*, 5527.

(2) Hosokawa, S.; Oshino, Y.; Tanabe, T.; Koga, H.; Beppu, K.; Asakura, H.; Teramura, K.; Motohashi, T.; Okumura, M.; Tanaka, T. Strong metal-support interaction in Pd/$Ca_2AlMnO_{5+\delta}$: catalytic NO reduction over Mn-doped CaO shell. *ACS Catal.* **2021**, *11*, 7996−8003.

(3) Beniya, A.; Higashi, S. Towards dense single-atom catalysts for future automotive applications. *Nat. Catal.* **2019**, *2*, 590−602.

(4) Zhang, Z.; He, G.; Li, Y.; Zhang, C.; Ma, J.; He, H. Effect of hydroxyl groups on metal anchoring and formaldehyde oxidation performance of Pt/Al_2O_3. *Environ. Sci. Technol.* **2022**, *56*, 10916−10924.

(5) Gao, P.; Chen, Z.; Gong, Y.; Zhang, R.; Liu, H.; Tang, P.; Chen, X.; Passerini, S.; Liu, J. The role of cation vacancies in electrode materials for enhanced electrochemical energy storage: Synthesis, advanced characterization, and fundamentals. *Adv. Energy Mater.* **2020**, *10*, 1903780.

(6) Xie, C.; Yan, D.; Li, H.; Du, S.; Chen, W.; Wang, Y.; Zou, Y.; Chen, R.; Wang, S. Defect chemistry in heterogeneous catalysis: recognition, understanding, and utilization. *ACS Catal.* **2020**, *10*, 11082−11098.

(7) Yan, Z.; Yao, B.; Hall, C.; Gao, Q.; Zang, W.; Zhou, H.; He, Q.; Zhu, H. Metal-metal oxide catalytic interface formation and structural evolution: A discovery of strong metal-support bonding, ordered intermetallics, and single atoms. *Nano Lett.* **2022**, *22*, 8122−8129.

(8) Kim, J.; Choi, H.; Kim, D.; Park, J. Y. Operando surface studies on metal-oxide interfaces of bimetal and mixed catalysts. *ACS Catal.* **2021**, *11*, 8645−8677.

(9) Huang, W.; Johnston-Peck, A. C.; Wolter, T.; Yang, W. C. D.; Xu, L.; Oh, J.; Reeves, B. A.; Zhou, C.; Holtz, M. E.; Herzing, A. A.; et al. Steam-created grain boundaries for methane C-H activation in palladium catalysts. *Science* **2021**, *373*, 1518−1523.

(10) Peng, L.; Peng, H.; Xu, L.; Wang, B.; Lan, K.; Zhao, T.; Che, R.; Li, W.; Zhao, D. Anisotropic self-assembly of asymmetric mesoporous hemispheres with tunable pore structures at liquid-liquid interfaces. *J. Am. Chem. Soc.* **2022**, *144*, 15754−15763.

(11) Duan, L.; Wang, C.; Zhang, W.; Ma, B.; Deng, Y.; Li, W.; Zhao, D. Interfacial assembly and applications of functional mesoporous materials. *Chem. Rev.* **2021**, *121*, 14349−14429.
(12) Jiang, Z.; Tian, M.; Jing, M.; Chai, S.; Jian, Y.; Chen, C.; Douthwaite, M.; Zheng, L.; Ma, M.; Song, W.; et al. Modulating the electronic metal-support interactions in single-atom Pt_1-CuO catalyst for boosting acetone oxidation. *Angew. Chem., Int. Ed.* **2022**, *61*, No. e202200763.
(13) Pu, T.; Zhang, W.; Zhu, M. Engineering heterogeneous catalysis with strong metal-support interactions: Characterization, theory and manipulation. *Angew. Chem., Int. Ed.* **2022**, *62*, No. e202212278.
(14) Xu, C.; Chen, G.; Zhao, Y.; Liu, P.; Duan, X.; Gu, L.; Fu, G.; Yuan, Y.; Zheng, N. Interfacing with silica boosts the catalysis of copper. *Nat. Commun.* **2018**, *9*, 3367.
(15) Zhang, J.; Wang, H.; Wang, L.; Ali, S.; Wang, C.; Wang, L.; Meng, X.; Li, B.; Su, D. S.; Xiao, F. S. Wet-chemistry strong metal-support interactions in titania-supported Au catalysts. *J. Am. Chem. Soc.* **2019**, *141*, 2975−2983.
(16) Peng, H.; Dong, T.; Yang, S.; Chen, H.; Yang, Z.; Liu, W.; He, C.; Wu, P.; Tian, J.; Peng, Y.; et al. Intra-crystalline mesoporous zeolite encapsulation-derived thermally robust metal nanocatalyst in deep oxidation of light alkanes. *Nat. Commun.* **2022**, *13*, 295.
(17) Li, D.; Xu, F.; Tang, X.; Dai, S.; Pu, T.; Liu, X.; Tian, P.; Xuan, F.; Xu, Z.; Wachs, I. E.; et al. Induced activation of the commercial $Cu/ZnO/Al_2O_3$ catalyst for the steam reforming of methanol. *Nat. Catal.* **2022**, *5*, 99−108.
(18) Chen, A.; Yu, X.; Zhou, Y.; Miao, S.; Li, Y.; Kuld, S.; Sehested, J.; Liu, J.; Aoki, T.; Hong, S.; et al. Structure of the catalytically active copper-ceria interfacial perimeter. *Nat. Catal.* **2019**, *2*, 334−341.
(19) Xu, M.; Qin, X.; Xu, Y.; Zhang, X.; Zheng, L.; Liu, J. X.; Wang, M.; Liu, X.; Ma, D. Boosting CO hydrogenation towards C^{2+} hydrocarbons over interfacial TiO_{2-x}/Ni catalysts. *Nat. Commun.* **2022**, *13*, 6720.
(20) Sun, X. C.; Yuan, K.; Hua, W. D.; Gao, Z. R.; Zhang, Q.; Yuan, C. Y.; Liu, H. C.; Zhang, Y. W. Weakening the metal-support interactions of M/CeO_2 (M = Co, Fe, Ni) using a NH_3-treated CeO_2 support for an enhanced water-gas shift reaction. *ACS Catal.* **2022**, *12*, 11942−11954.
(21) Zhang, Y.; Zhang, J.; Zhang, B.; Si, R.; Han, B.; Hong, F.; Niu, Y.; Sun, L.; Li, L.; Qiao, B.; et al. Boosting the catalysis of gold by O_2 activation at Au-SiO_2 interface. *Nat. Commun.* **2020**, *11*, 558.
(22) Wang, C.; Liu, S.; Wang, D.; Chen, Q. Interface engineering of Ru-Co_3O_4 nanocomposites for enhancing CO oxidation. *J. Mater. Chem. A* **2018**, *6*, 11037−11043.
(23) He, M.; Cao, Y.; Ji, J.; Li, K.; Huang, H. Superior catalytic performance of Pd-loaded oxygen-vacancy-rich TiO_2 for formaldehyde oxidation at room temperature. *J. Catal.* **2021**, *396*, 122−135.
(24) Ma, C.; Sun, S.; Lu, H.; Hao, Z.; Yang, C.; Wang, B.; Chen, C.; Song, M. Remarkable MnO_2 structure-dependent H_2O promoting effect in HCHO oxidation at room temperature. *J. Hazard. Mater.* **2021**, *414*, 125542.
(25) Chen, X.; He, G.; Li, Y.; Chen, M.; Qin, X.; Zhang, C.; He, H. Pathway for Dioxymethylene conversion to formate catalyzed by surface hydroxyl on TiO_2-based catalyst. *ACS Catal.* **2020**, *10*, 9706−9715.
(26) Polo-Garzon, F.; Blum, T. F.; Bao, Z.; Wang, K.; Fung, V.; Huang, Z.; Bickel, E. E.; Jiang, D.-e.; Chi, M.; Wu, Z. In situ strong metal-support interaction (SMSI) affects catalytic alcohol conversion. *ACS Catal.* **2021**, *11*, 1938−1945.
(27) Luo, Z.; Zhao, G.; Pan, H.; Sun, W. Strong metal-support interaction in heterogeneous catalysts. *Adv. Energy Mater.* **2022**, *12*, 2201395.
(28) Liu, J.; Wang, L.; Okejiri, F.; Luo, J.; Zhao, J.; Zhang, P.; Liu, M.; Yang, S.; Zhang, Z.; Song, W.; et al. Deep understanding of strong metal interface confinement: A journey of Pd/FeO_x catalysts. *ACS Catal.* **2020**, *10*, 8950−8959.
(29) Zhang, J.; Qin, X.; Chu, X.; Chen, M.; Chen, X.; Chen, J.; He, H.; Zhang, C. Tuning metal-support interaction of Pt-CeO_2 Catalysts for enhanced oxidation reactivity. *Environ. Sci. Technol.* **2021**, *55*, 16687−16698.
(30) Wang, H.; Wang, L.; Lin, D.; Feng, X.; Niu, Y.; Zhang, B.; Xiao, F. S. Strong metal-support interactions on gold nanoparticle catalysts achieved through Le Chatelier's principle. *Nat. Catal.* **2021**, *4*, 418−424.
(31) Datka, J.; Gil, B.; Baran, P. Heterogeneity of OH groups in HZSM-5 zeolites: splitting of OH and OD bands in low-temperature IR spectra. *Microporous Mesoporous Mater.* **2003**, *58*, 291−294.
(32) Liu, F.; Liu, X.; Shen, J.; Bahi, A.; Zhang, S.; Wan, L.; Ko, F. The role of oxygen vacancies on Pt/$NaInO_2$ catalyst in improving formaldehyde oxidation at ambient condition. *Chem. Eng. J.* **2020**, *395*, 125131.
(33) Li, Y.; Zhang, C.; Ma, J.; Chen, M.; Deng, H.; He, H. High temperature reduction dramatically promotes Pd/TiO_2 catalyst for ambient formaldehyde oxidation. *Appl. Catal., B* **2017**, *217*, 560−569.
(34) Kadja, G. T. M.; Suprianti, T. R.; Ilmi, M. M.; Khalil, M.; Mukti, R. R.; Subagjo. Sequential mechanochemical and recrystallization methods for synthesizing hierarchically porous ZSM-5 zeolites. *Microporous Mesoporous Mater.* **2020**, *308*, 110550.
(35) Dai, Q.; Bai, S.; Wang, X.; Lu, G. Facile synthesis of HZSM-5 with controlled crystal morphology and size as efficient catalysts for chlorinated hydrocarbons oxidation and xylene isomerization. *J. Porous Mater.* **2014**, *21*, 1041−1049.
(36) Di, Z.; Chen, H.; Zhang, R.; Wang, H.; Jia, J.; Wei, Y. Significant promotion of reducing treatment on Pd/TS-1 zeolite for formaldehyde catalytic purification at ambient temperature. *Appl. Catal., B* **2022**, *304*, 120843.
(37) Muravev, V.; Spezzati, G.; Su, Y. Q.; Parastaev, A.; Chiang, F. K.; Longo, A.; Escudero, C.; Kosinov, N.; Hensen, E. J. M. Interface dynamics of Pd-CeO_2 single-atom catalysts during CO oxidation. *Nat. Catal.* **2021**, *4*, 469−478.
(38) Xu, H.; Zhang, Z.; Liu, J.; Do-Thanh, C. L.; Chen, H.; Xu, S.; Lin, Q.; Jiao, Y.; Wang, J.; Wang, Y.; et al. Entropy-stabilized single-atom Pd catalysts via high-entropy fluorite oxide supports. *Nat. Commun.* **2020**, *11*, 3908.
(39) Yang, X.; Li, Q.; Lu, E.; Wang, Z.; Gong, X.; Yu, Z.; Guo, Y.; Wang, L.; Guo, Y.; Zhan, W.; et al. Taming the stability of Pd active phases through a compartmentalizing strategy toward nanostructured catalyst supports. *Nat. Commun.* **2019**, *10*, 1611.
(40) Eblagon, K. M.; Concepción, P. H.; Silva, H.; Mendes, A. Ultraselective low temperature steam reforming of methanol over PdZn/ZnO catalysts—Influence of induced support defects on catalytic performance. *Appl. Catal., B* **2014**, *154*−*155*, 316−328.
(41) Rameshan, C.; Stadlmayr, W.; Weilach, C.; Penner, S.; Lorenz, H.; Hävecker, M.; Blume, R.; Rocha, T.; Teschner, D.; Knop-Gericke, A.; et al. Subsurface-controlled CO_2 selectivity of PdZn near-surface alloys in H_2 generation by methanol steam reforming. *Angew. Chem., Int. Ed.* **2010**, *49*, 3224−3227.
(42) Sun, Q.; Chen, B. W. J.; Wang, N.; He, Q.; Chang, A.; Yang, C. M.; Asakura, H.; Tanaka, T.; Hülsey, M. J.; Wang, C. H.; et al. Zeolite-Encaged Pd-Mn Nanocatalysts for CO_2 Hydrogenation and Formic Acid Dehydrogenation. *Angew. Chem., Int. Ed.* **2020**, *132*, 20358−20366.
(43) Sun, Q.; Wang, N.; Bing, Q.; Si, R.; Liu, J.; Bai, R.; Zhang, P.; Jia, M.; Yu, J. Subnanometric hybrid Pd-$M(OH)_2$, M= Ni, Co, clusters in zeolites as highly efficient nanocatalysts for hydrogen generation. *Chem* **2017**, *3*, 477−493.
(44) Sadi, F.; Duprez, D.; Gérard, F.; Miloudi, A. Hydrogen formation in the reaction of steam with Rh/CeO_2 catalysts: a tool for characterising reduced centres of ceria. *J. Catal.* **2003**, *213*, 226−234.
(45) Wang, L.; Zhang, L.; Zhang, L.; Yun, Y.; Wang, K.; Yu, B.; Zhao, X.; Yang, F. Direct environmental TEM observation of silicon diffusion-induced strong metal-silica interaction for boosting CO_2 hydrogenation. *Nano Res.* **2023**, *16*, 2209−2217.
(46) Yang, F.; Zhao, H.; Wang, W.; Wang, L.; Zhang, L.; Liu, T.; Sheng, J.; Zhu, S.; He, D.; Lin, L.; et al. Atomic origins of the strong

https://doi.org/10.1021/jacsau.3c00093
JACS Au 2023, 3, 1230−1240

metal-support interaction in silica supported catalysts. *Chem. Sci.* **2021**, *12*, 12651−12660.
(47) Wang, J.; Fu, Y.; Kong, W.; Li, S.; Yuan, C.; Bai, J.; Chen, X.; Zhang, J.; Sun, Y. Investigation of atom-level reaction kinetics of carbon-resistant bimetallic NiCo-reforming catalysts: Combining microkinetic modeling and density functional theory. *ACS Catal.* **2022**, *12*, 4382−4393.
(48) Liu, Y. R.; Li, X.; Liao, W. M.; Jia, A. P.; Wang, Y. J.; Luo, M. F.; Lu, J. Q. Highly active Pt/BN catalysts for propane combustion: The roles of support and reactant-induced evolution of active sites. *ACS Catal.* **2019**, *9*, 1472−1481.
(49) Oyama, S.; Zhang, X.; Lu, J.; Gu, Y.; Fujitani, T. Epoxidation of propylene with H_2 and O_2 in the explosive regime in a packed-bed catalytic membrane reactor. *J. Catal.* **2008**, *257*, 1−4.
(50) Dong, T.; Liu, W.; Ma, M.; Peng, H.; Yang, S.; Tao, J.; He, C.; Wang, L.; Wu, P.; An, T. Hierarchical zeolite enveloping Pd-CeO_2 nanowires: An efficient adsorption/catalysis bifunctional catalyst for low temperature propane total degradation. *Chem. Eng. J.* **2020**, *393*, 124717.
(51) Zou, Z. Q.; Meng, M.; Li, Q.; Zha, Y. Q. Surfactants-assisted synthesis and characterizations of multicomponent mesoporous materials Co-Ce-Zr-O and Pd/Co-Ce-Zr-O used for low-temperature CO oxidation. *Mater. Chem. Phys.* **2008**, *109*, 373−380.
(52) Yue, B.; Zhou, R.; Wang, Y.; Zheng, X. Study of the methane combustion and TPR/TPO properties of Pd/Ce-Zr-M/Al_2O_3 catalysts with M=Mg, Ca, Sr, Ba. *J. Mol. Catal. A: Chem.* **2005**, *238*, 241−249.
(53) Soria, J.; Martínez-Arias, A.; Coronado, J. M.; Conesa, J. C. Electron paramagnetic resonance spectroscopy study of the adsorption of O_2 and CO on a Pt/CeO_2/AI_20_3 catalyst. *Colloids Surf. A Physicochem. Eng. Asp.* **1996**, *115*, 215−221.
(54) Sun, Y.; Xu, J.; Xu, X.; Fang, X.; Guo, Y.; Liu, R.; Zhong, W.; Wang, X. Tailoring active O_2^- and O_2^{2-} anions on a ZnO surface with the addition of different alkali metals probed by CO oxidation. *Ind. Eng. Chem. Res.* **2020**, *59*, 9382−9392.
(55) Chen, M.; Qiu, Y.; Wang, W.; Li, X.; Wang, J.; Wen, H.; Yang, Z.; Wang, P. Engineering oxygen vacancies via amorphization in conjunction with W-doping as an approach to boosting catalytic properties of Pt/Fe-W-O for formaldehyde oxidation. *J. Hazard. Mater.* **2021**, *416*, 126224.
(56) Ye, J.; Zhou, M.; Le, Y.; Cheng, B.; Yu, J. Three-dimensional carbon foam supported MnO_2/Pt for rapid capture and catalytic oxidation of formaldehyde at room temperature. *Appl. Catal., B* **2020**, *267*, 118689.
(57) Li, N.; Huang, B.; Dong, X.; Luo, J.; Wang, Y.; Wang, H.; Miao, D.; Pan, Y.; Jiao, F.; Xiao, J.; et al. Bifunctional zeolites-silver catalyst enabled tandem oxidation of formaldehyde at low temperatures. *Nat. Commun.* **2022**, *13*, 2209.
(58) Huang, M.; Li, Y.; Li, M.; Zhao, J.; Zhu, Y.; Wang, C.; Sharma, V. K. Active site-directed tandem catalysis on single platinum nanoparticles for efficient and stable oxidation of formaldehyde at room temperature. *Environ. Sci. Technol.* **2019**, *53*, 3610−3619.
(59) Li, Y.; Chen, X.; Wang, C.; Zhang, C.; He, H. Sodium enhances Ir/TiO_2 activity for catalytic oxidation of formaldehyde at ambient temperature. *ACS Catal.* **2018**, *8*, 11377−11385.
(60) Sun, X.; Lin, J.; Guan, H.; Li, L.; Sun, L.; Wang, Y.; Miao, S.; Su, Y.; Wang, X. Complete oxidation of formaldehyde over TiO_2 supported subnanometer Rh catalyst at ambient temperature. *Appl. Catal., B* **2018**, *226*, 575−584.
(61) Jiang, G.; Su, Y.; Li, H.; Chen, Y.; Li, S.; Bu, Y.; Zhang, Z. Insight into the Ag-CeO_2 interface and mechanism of catalytic oxidation of formaldehyde. *Appl. Surf. Sci.* **2021**, *549*, 149277.
(62) Wang, C.; Li, Y.; Zhang, C.; Chen, X.; Liu, C.; Weng, W.; Shan, W.; He, H. A simple strategy to improve Pd dispersion and enhance Pd/TiO_2 catalytic activity for formaldehyde oxidation: The roles of surface defects. *Appl. Catal., B* **2021**, *282*, 119540.
(63) Chen, X.; Chen, M.; He, G.; Wang, F.; Xu, G.; Li, Y.; Zhang, C.; He, H. Specific role of potassium in promoting Ag/Al_2O_3 for catalytic oxidation of formaldehyde at low temperature. *J. Phys. Chem. C* **2018**, *122*, 27331−27339.
(64) Sun, X.; Lin, J.; Wang, Y.; Li, L.; Pan, X.; Su, Y.; Wang, X. Catalytically active Ir^0 species supported on Al_2O_3 for complete oxidation of formaldehyde at ambient temperature. *Appl. Catal., B* **2020**, *268*, 118741.

https://doi.org/10.1021/jacsau.3c00093
JACS Au 2023, 3, 1230−1240